Subcontinuum structures of reactive shock waves in gaseous H_2/O_2 mixtures

Thibault Maurel-Oujia [*] and Kazuki Maeda [†]
School of Aeronautics and Astronautics, Purdue University, West Lafayette, Indiana 47907, USA

(Received 19 February 2025; accepted 22 August 2025; published 15 October 2025)

We present a molecular dynamics simulation of a Mach 5 reactive shock wave in a stoichiometric gaseous H_2/O_2 mixture. H_2 is compressed slightly ahead of O_2 to form two separate shock fronts. Chemical reactions initiate during the O_2 compression, followed by a postdetonation flow exhibiting a Zeldovich–von Neumann–Döring-like structure. To analyze the shock substructure, the profiles of state variables near the shock and the postshock particle velocities of molecules are compared with those of a synthetic, inert shock wave. The results indicate that the small H_2 to O_2 mass ratio causes the separation of shock fronts regardless of chemistry, like those observed in rarefied binary gases, and the velocities of the species relax before leaving the shock region, characterizing the nonequilibrium H_2/O_2 shock dynamics so that reactions are present but not as active as they were without the separation.

DOI: 10.1103/y7lz-563m

I. INTRODUCTION

The shock-induced chemical reaction (SICR) of energetic gases is of critical importance for various applications, including power and transportation, high-pressure propulsion, and chemical synthesis [1–15]. Among the various gases, hydrogen is attracting considerable attention as a renewable fuel source [8,9,16–20]. In SICR, the rapid compression and heating of reactant gases by shock waves can lead to explosive ignition. Understanding the coupled physics of reaction and fluid dynamics is challenging due to the multiscale and nonequilibrium nature of the shock wave with the thickness, as small as the molecular mean free path, propagating at a supersonic speed.

Models of gaseous shock waves have been explored extensively through continuum and kinetic theories based on the Navier-Stokes equations [21–24] and Boltzmann-type equations [25–37]. Boltzmann-type methods, including direct simulation Monte Carlo (DSMC), are capable of capturing nonequilibrium gas dynamics beyond the reach of continuum models. These methods and variants have been used to simulate SICR of endothermic dissociation in high-speed rarefied gas flows [33–35]. Application to SICR of exothermic combustion has been highly limited except for recent studies for H_2/O_2 mixtures [38–40]. Detailed subcontinuum shock structures have not been reported yet. In general, DSMC requires special attention to ensure convergence in near-continuum flows [41] as well as to express recombination chemistry. Consequently, capturing the SICR of energetic gases below the continuum scale remains a challenge.

With increasing computing power, it has become feasible to address shock dynamics at the continuum scale by using first-principles molecular dynamics (MD) simulations. MD was used to examine shock-induced structural and dynamic changes in condensed materials [42–46]. In particular, SICR pathways and dynamic phase changes were simulated in condensed energetic

[*]Contact author: tmaurelo@purdue.edu
[†]Contact author: kmaeda@purdue.edu

materials [47–52]. In addition, MD techniques have been applied to shock waves in gases, such as an idealized hard-sphere gas [53], Lennard-Jones monatomic and diatomic gases [54], and shocked air with endothermic dissociation [55] including the effects of vibrational-translational nonequilibrium. Nevertheless, MD of the SICR in realistic energetic gases has remained largely unexplored.

Here, we present the reactive MD simulation of SICR by a Mach 5 shock wave driven by a moving piston in a square duct filled with a gaseous stoichiometric H_2/O_2 mixture initially quiescent at 1 atm and 500 K. Chemical reactions are modeled using the ReaxFF potential [56]. Since simulation of the timescale over which the shock reaches its stationary state remains computationally prohibitive, we focus on the period of ignition until the shock speed becomes approximately stabilized. After ignition, the simulated MD field resembles the familiar one-dimensional ZND (Zeldovich–von Neumann–Döring [57–59]) profile of detonation waves at the continuum scale, while presenting the clear separation of the shock front of H_2 and that of O_2 within the mixture's shock wave; H_2 is compressed ahead of O_2 to cause the local fluctuation of the mixture ratio. Reaction products are observed near and behind the H_2 shock front. To isolate the effect of reactions on the shock structure, the same shock wave is simulated without H-O chemistry. This synthetic case presents a lower shock speed as a result of the absence of exothermic heat release, but the shock wave has a similar structure of separation. The separation can be associated with previous models of shock waves of inert binary mixtures with a large mass ratio, exhibiting similar shock structures due to anisotropic diffusion. Furthermore, the MD data show that, in both reactive and inert cases, the H and O atoms initially present ballistic velocities greater than and smaller than the shock speed of the mixture. This species nonequilibrium is relaxed in the shock region before the mixture's velocity is relaxed to the theoretical, Rankine-Hugoniot postshock value. These results indicate multiscale physics in which the large difference in the postshock, nonequilibrium velocities of H_2 and O_2 due to their distinct molecular masses creates the microscopic shock front separation that can suppress chemical reactions within and further downstream of the shock at larger scales.

II. METHODOLOGY

Reactive molecular dynamics (MD) simulations were conducted with LAMMPS [60] employing the ReaxFF potential [56] to simulate the dynamic behavior of molecules, including reactants, radicals, and products, in response to high-velocity shocks driven by a moving piston. ReaxFF accurately models bond formation and dissociation. The domain was initially filled with a stoichiometric H_2/O_2 mixture at $P_0 = 1$ atm and $T_0 = 500$ K, with zero mean velocity. Each molecule is tracked in time t in a rectangular domain in x-y-z Cartesian coordinates, with the shock wave propagating in the $+z$ direction away from a moving piston initially at $z = 0$. The dimension of the x-y cross section is $0.025 \times 0.025\,\mu m^2$. The x and y domain boundaries are periodic. The $+z$ domain boundary is modeled as an adiabatic wall. To accommodate the propagation of the shock wave without interference from boundary effects, the domain length in the z-direction, L_z, was dynamically extended by adding additional segments as the shock approached the domain boundaries. The initial value of L_z is 10 μm.

The piston is initially positioned at the $-z$ domain boundary. The piston speed is set constant at $2175.18\,m\,s^{-1}$ to collide with molecules to generate a shock wave. For the stoichiometric H_2/O_2 mixture, the shock speed driven by this piston velocity calculated under ideal gas assumptions and in the absence of chemical reactions was found to be $2784.51\,m\,s^{-1}$, corresponding to Mach 4. The evolution of atomic distributions was tracked over 24 ns after the shock formation.

The simulations were conducted using the CHO-2008 force field [61]. The system was first energy-minimized using the conjugate-gradient algorithm. It was then equilibrated for 25 ps in the canonical ensemble (*NVT*) at 500 K using a Nosé-Hoover thermostat [62] (damping time of 100 fs). During the *NVT* phase, reactions were deactivated. Following this, MD simulations were performed under a microcanonical ensemble (*NVE*). A time step of 0.2 fs was used for both the *NVT* and *NVE* simulations. Time integration was performed using the velocity-Verlet algorithm [63].

Our transverse domain is several orders of magnitude smaller than the typical cell size of a stoichiometric H_2/O_2 detonation. Experimental measurements at 1 atm and 293 K report a detonation cell size of approximately 1 mm [64–68]. Performing three-dimensional MD simulations over millimeter scale domains incurs prohibitive computational cost. Therefore, our study is focused on a one-dimensional, atomically resolved investigation of the shock front and the early stages of shock formation, without attempting to reproduce the macroscopic cellular structure of the detonation.

In the remainder of this article, streamwise velocities are calculated using the mass-weighted formulation [29]

$$v_z^{\mathrm{mix}} = \frac{\sum_i m_i N_i v_{z,i}}{\sum_i m_i N_i}, \tag{1}$$

where m_i and N_i are the mass of the molecule and the number density of species i, respectively, and $v_{z,i}$ is the velocity of the molecule i in the z direction. This formulation ensures that heavier molecules contribute proportionally more to the bulk velocity, reflecting their greater momentum.

The translational temperature is computed based on the molecular kinetic energy using the relation

$$T = \frac{2}{3k_B}\left\langle \frac{1}{2} m_i \boldsymbol{v}_i'^2 \right\rangle, \tag{2}$$

where k_B is the Boltzmann constant, m_i is the mass of the molecule, and $\boldsymbol{v}_i'$ denotes the velocity fluctuation relative to the local mean velocity.

We define the weighted number density of molecules as $\widetilde{N}_X\, p(N_X)$, where $\widetilde{N}_X$ and $p(N_X)$ are the weighting factor and the probability (number) density of species X at position z, respectively. The weighting factor is defined as $\widetilde{N}_X = N_{X,m} N_{X,a}$ to represent the total number of atoms in species X in the domain, where $N_{X,m}$ is the total number of molecules of X, and $N_{X,a}$ is the number of all atoms per molecule (equal to 1 for single-atom molecules).

III. RESULTS

A. Shock evolution

Figures 1(a)–1(d) show the space-time contour diagrams of the weighted number density for representative reactant and product species. We observe the formation of the initial shock generated by the piston propagating at a constant speed, followed by the emergence of radicals and products at approximately 4 ns. Additionally, after 10 ns, H_2 and O_2 are reduced from the shocked region and are predominantly present at the shock front. Approximately at 12 ns, the density at the shock front reaches its maximum, and subsequently the shock accelerates, as indicated by the change in the inclination of the curve in the figure. The density at the shock decreases thereafter, and by around 16 ns the species concentration ratios at the shock front seem stabilized. Figure 2 shows the evolution of the shock speed. We observe that the shock speed is transitioning from 2630 to 3500 m s^{-1}, between $t = 8$ and 16 ns. This transition corresponds to the emergence of the overdrive detonation wave.

Figure 2 further shows that the shock velocity does not actually stabilize but rather decreases continuously from the maximum value of 3544.30 m s^{-1} at 17.3 ns to 3432.26 m s^{-1} at 24 ns. The present piston-driven reactive shock wave is considered as an overdriven detonation wave, in which the detonation parameters exceed the corresponding Chapman-Jouguet values. As a reference, the wave speed of the steady, ZND detonation wave driven by the present piston speed for stoichiometric H_2/O_2 at 500 K and 1 atm, computed with the Hong *et al.* [69] mechanism in the SDToolbox [70], is 3185 m s^{-1} at the overdriven factor of 1.15.

The present shock speed after ignition is thus faster than the wave speed of the steady, overdriven ZND solution by 8%. This difference can be explained by the overcompression of the postshock region between the piston and the shock. The present postshock length is only 20 nm, and this is

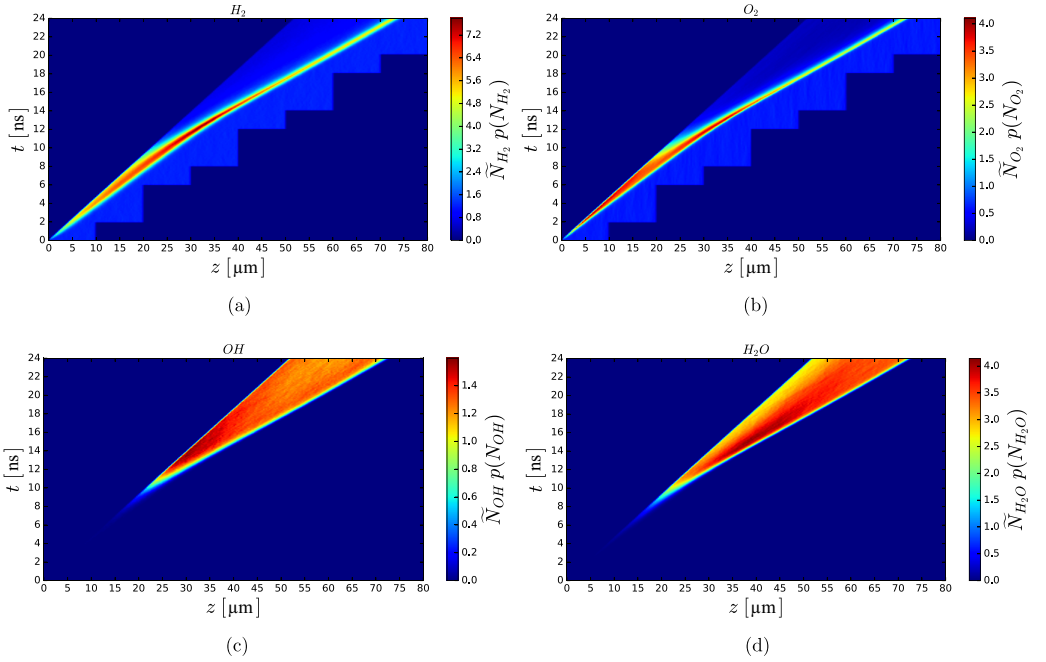

FIG. 1. Contour of the space-time distribution for each species in a reactive H_2/O_2 mixture during 24 ns for (a) H_2, (b) O_2, (c) OH, and (d) H_2O.

much shorter than the length scale of the pressure decay in the steady solution of more than 60 nm (Appendix A).

We expect that, once the piston becomes distant from the shock, the postshock pressure is lowered and the postshock state approaches the steady solution. Achieving the steady state in the MD simulation would require a simulation time much longer than the present 24 ns, and it can become prohibitively expensive. However, since the offset of the present wave speed from the steady solution is small and the transient decay of the wave speed is smooth, we also expect that the structure of the shock region is already stabilized and holds up to the steady state.

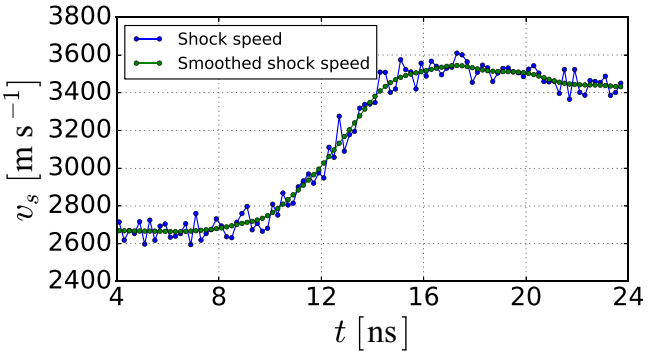

FIG. 2. Evolution of the shock speed in the reactive H_2/O_2 mixture, showing both the raw data (blue) and the smoothed data (green).

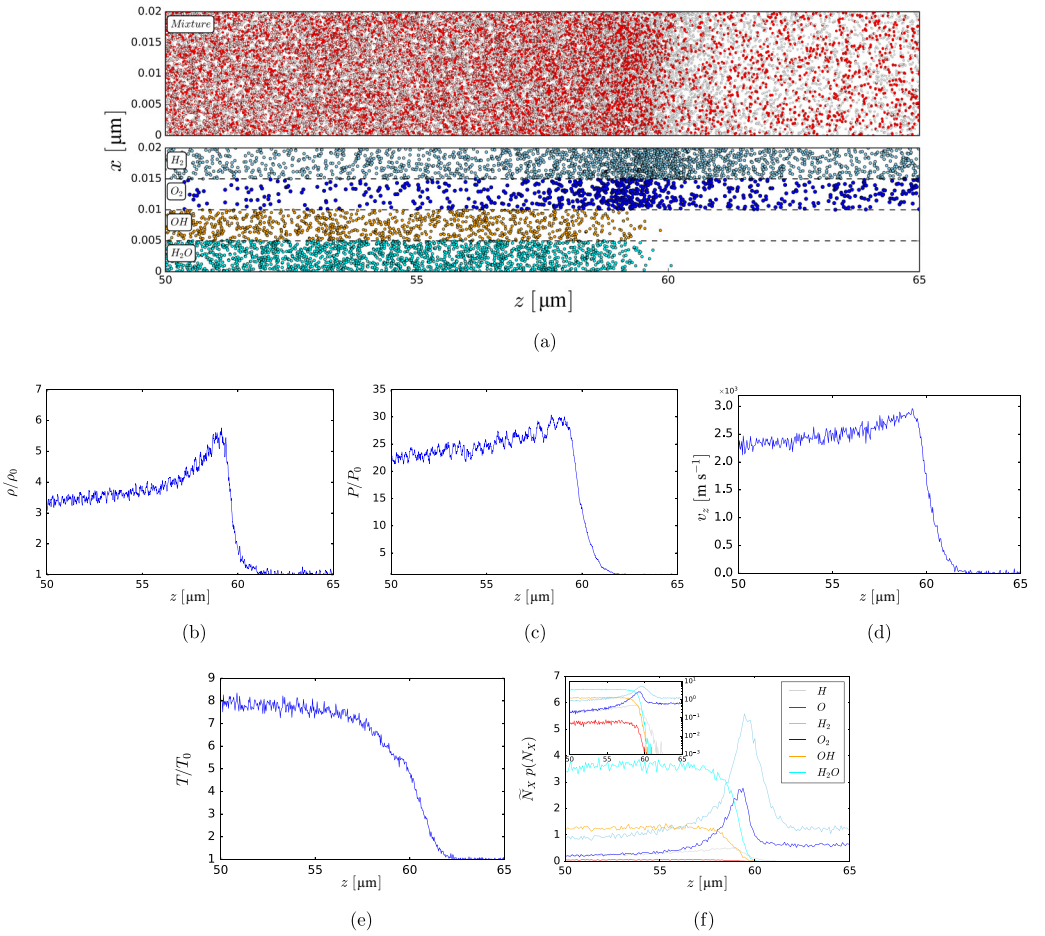

FIG. 3. (a) Visualization of molecular distributions on the xz-plane with a thickness along the y-axis of 2×10^{-3} μm at $t = 20$ ns for the reactive H_2/O_2 case. In the upper panel, all species are displayed in a combined view with each atom plotted individually. In the lower panel, the distributions of H_2, O_2, OH, and H_2O are shown, with each molecule represented by a single point located at its center of mass. (b) Density, (c) pressure, (d) velocity, and (e) temperature profile. (f) Corresponding species distribution histogram, where $p(N_X)$ represents the probability density of species X at position z, weighted by the total atoms per species $\widetilde{N}_X = N_{X,m} N_{X,a}$, with $N_{X,m}$ being the total number of molecules of X, and $N_{X,a}$ is the number of all atoms per molecule. The inset shows the same curve plotted on a logarithmic scale.

B. Stratified shock structure

The visualization of the reactive MD simulation is shown in Fig. 3(a) at $t = 20$ ns. The upper panel presents a combined view of all species, where the H and O atoms are colored gray and red. The shock wave is evident at $z \approx 60$ μm, where the molecular density is high. In the postshock region ($-z$ side of the shock-region), the density decreases slightly with distance from the shock front. The lower panel shows the distributions of major species H_2, O_2, OH, and H_2O, with each molecule represented by a single point at its center of mass. All visualizations correspond to a projected view of the thin slice of thickness 2×10^{-3} μm along the y-axis. In the preshock region at $z \gtrapprox 60$ μm, the density of H_2 and O_2 remains comparatively low and uniform. At $z \lessapprox 60$ μm, the shock region of the mixture exhibits a significantly higher density. The densities of both species in the postshock region are smaller than those in the preshock region, and mildly decrease with

distance from the shock. Interestingly, the dense region of H_2 is positioned at $z \approx 60\,\mu$m, slightly ahead of that of O_2 at $z \approx 59\,\mu$m. OH and H_2O appear behind the shock region. Strong density gradients for OH and H_2O are not observed in the postshock region.

The mixture density, pressure, streamwise mass-weighted velocity, and translational temperature along the z-axis are obtained from the data of Fig. 3(a) [Figs. 3(b)–3(e)]. The variables are normalized by the preshock values denoted by $(\cdot)_0$. The shock speed is $3504.55\,\mathrm{m\,s^{-1}}$ at $t = 20\,$ns (Fig. 2). The plots are overall consistent with the visualization. As expected, the profiles in these plots resemble the ZND structure. Further details on the comparisons with steady ZND solutions are provided in Appendix A.

All variables remain flat in the preshock region and present steep gradients in the shock region. In the postshock region, density, pressure, and velocity decay and the temperature increases with distance from the shock wave. This temperature increase is attributed to exothermic heat release in the postshock region. The shock thickness is $\delta \approx 1.17\,\mu$m, where δ is defined as $\delta = -(v_{z,a} - v_{z,b})/(\frac{dv_z}{dz})_{\min}$ [71]. In this expression, $v_{z,a}$ and $v_{z,b}$ represent the velocities immediately upstream and downstream of the shock, respectively, while $(\frac{dv_z}{dz})_{\min}$ denotes the minimum slope of the velocity across the shock wave. The weighted number density of molecules, $\widetilde{N}_X\, p(N_X)$, along the z-axis, is shown in Fig. 3(f) for major chemical species. The offset of the H_2 and O_2 shock fronts is clear in this plot. Radicals and reaction products emerge mostly behind the H_2 shock front and fully overlap with the O_2 shock front. Notably, H radicals appear with the H_2 shock front, while O and OH radicals appear in the upstream along with the O_2 shock front, highlighting that the shock-induced collisional enhancement within the shock front of each species drives corresponding endothermic dissociation reactions. The early appearance of H radicals indicates that they are ready to recombine with OH to form H_2O as soon as OH appears. In fact, H_2O appears with the OH and O radicals without delay. In the postshock region, the fraction of products species rapidly saturate and those of the radicals disappear with distance from the shock. Thus, chemical reactions are indicated to occur within the shock region, as opposed to continuum theories that typically assume no chemical reactions within the shock region, but the amount of reactions may be insignificant. The potential overlap of shock and reaction zones was also pointed out in a previous study using MD [53]. Our conjecture is that, in the present H_2/O_2 mixture, the reaction in the shock region may be limited by the local nonstoichiometric conditions created by the separation of the H_2 and O_2 shock fronts.

C. Comparisons with a synthetic inert shock wave

Further analysis of the interplay of reactions and the shock structure can be cumbersome due to simultaneous collision and reaction dynamics. Comparisons with a shock wave without reactions may enable us to isolate the effect of reactions on the separation. To this end, we simulate the same parameters as the H_2/O_2 shock wave, but with artificially deactivated chemical reactions. The space-time contour diagrams of the inert shock are presented in Appendix B.

1. Species distribution and velocity profiles

The distributions of H_2 and O_2, and the ratio N_{H_2} to N_{O_2}, $p(N_{H_2}/N_{O_2})$, are shown in Figs. 4(a) and 4(b) for both reactive (a) and inert (b) cases. The ratio N_H to N_O contained in all species $[p(N_H/N_O)]$ is also plotted in the reactive case [Fig. 4(a)] to account for the effect of consumption of H_2 and O_2. The translational velocities are shown in Figs. 4(c) and 4(d). The shock speed in the inert case is found to be $2630.51\,\mathrm{m\,s^{-1}}$, smaller than that of the reactive case, as expected due to the absence of exothermic heat release. The inert postshock velocities remain constant at values lower than the reactive case. Up to the tail of the O_2 shock front from the shock upstream, the distributions of the plotted variables are similar between the two cases. The ratio $p(N_{H_2}/N_{O_2})$ varies with H_2 in the H_2 shock front and peaks within the shock wave [Figs. 4(a) and 4(b)], locally creating an

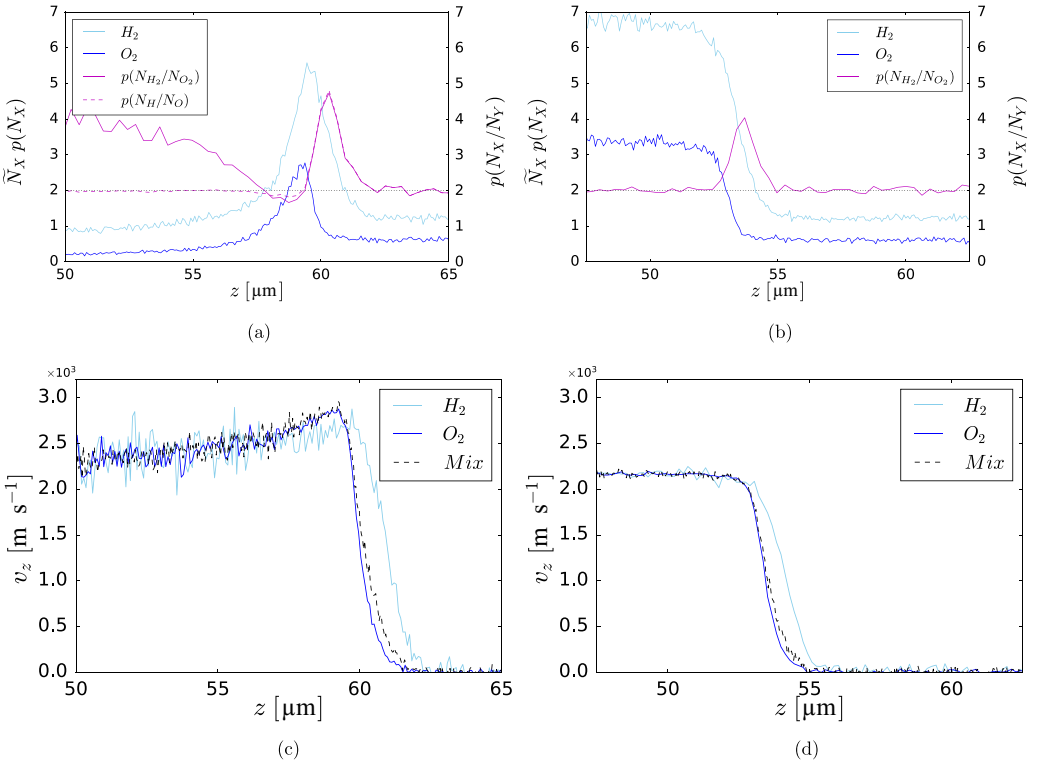

FIG. 4. Comparisons of (a),(c) reactive and (b),(d) inert H_2/O_2 mixtures at $t = 20$ ns. (a),(b) Species distribution showing the number of H_2 and O_2 molecules and their relative ratio $p(N_{H_2}/N_{O_2}) = \widetilde{N}_{H_2} p(N_{H_2})/\widetilde{N}_{O_2} p(N_{O_2})$, and (c),(d) velocity profiles for H_2 and O_2, as well as the mass-weighed velocity of the mixture.

H_2 rich condition. The growth of the velocity of H_2 is offset by $O(1)$ μm upstream of that of O_2 [Figs. 4(c) and 4(d)]. The similarity of the two cases indicates that the shock separation is due to the dynamics of the binary mixture but not directly to reactions. Such shock structures in rarefied binary mixtures have been extensively studied using continuum and kinetic models [23,29,72], and they are attributed to anisotropic diffusion that drives light gases to diffuse faster than heavier gases in the mixture.

The regions of the shock-tail and the postshock regions present significant differences between the reactive and inert cases. In the reactive case, behind their peaks within the shock wave, both $p(N_{H_2}/N_{O_2})$ and $p(N_H/N_O)$ show a rapid decrease with the increase in O_2 and drop below 2 at $z \approx 59$ μm. In the postshock region, $p(N_H/N_O)$ immediately recovers 2 but $p(N_{H_2}/N_{O_2})$ increases with distance from the shock wave In the inert case, $p(N_{H_2}/N_{O_2})$ also drops with increasing O_2 but without undershoot. These differences are now attributed to chemical reactions. The undershoot of $p(N_{H_2}/N_{O_2})$ and $p(N_H/N_O)$ can be explained by the reaction within the shock. At $z \approx 60$ μm, H_2 in the reactive case peaks at $\widetilde{N}_{H_2} p(N_{H_2}) \approx 5.5$, smaller than the inert postshock value [$\widetilde{N}_{H_2} p(N_{H_2}) \approx 7$], despite the greater shock strength. In agreement with the visualization [Fig. 3(a)], the consumption of H_2 and the exothermic expansion of radicals and products thus begin at the H_2 shock front, even during compression of O_2, creating locally the O_2-rich region. The slight positive offset of the velocity peak of H_2 from that of O_2 at $z \approx 60$ μm in Fig. 4(c) also supports the argument that the compression of H_2 terminates during the compression of O_2. The large values of $p(N_{H_2}/N_{O_2})$ at $z \lessapprox 57$ μm are due to the relatively higher molar consumption of O_2 than H_2 in the postshock reaction ($2H_2 + O_2 \rightarrow 2OH + H_2$). The mixture's shock thickness of the inert case is approximately

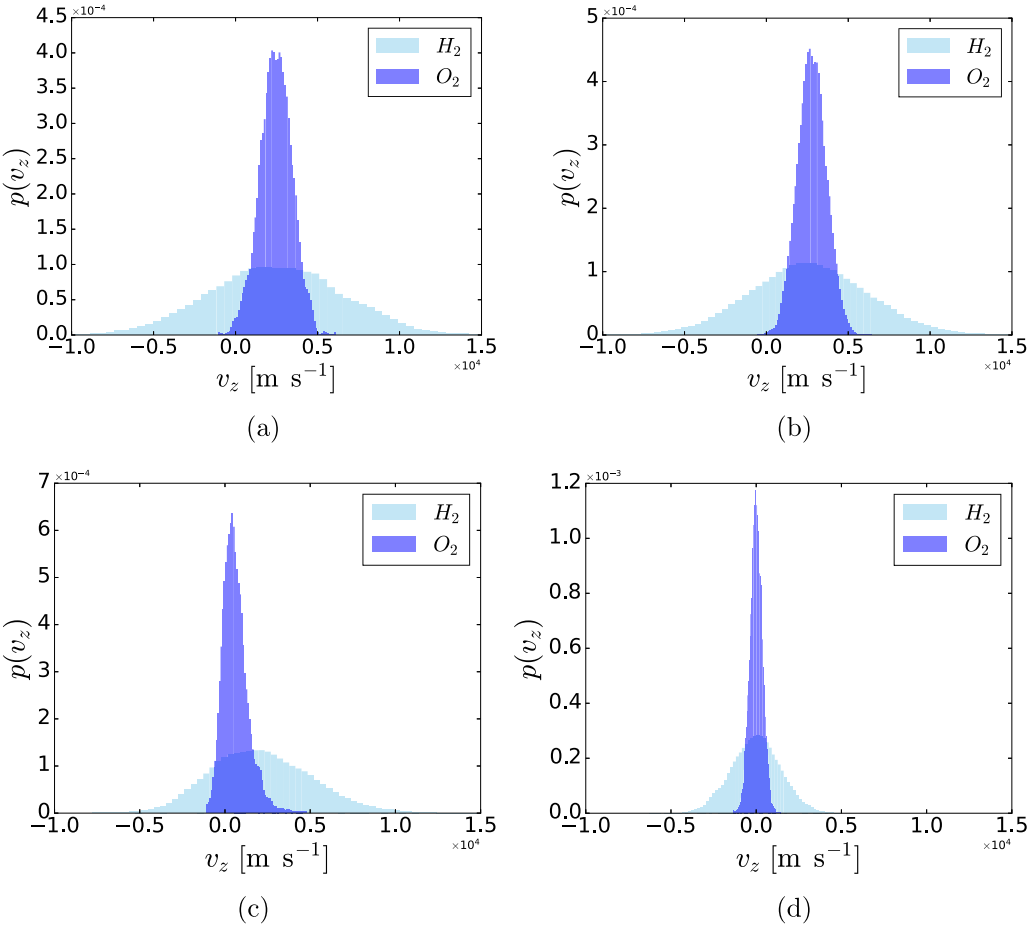

FIG. 5. Velocity distribution in the z direction of the center of mass for H_2 and O_2 in the reactive case (a) downstream of the shock front; (b) immediately after the shock, where a demixing effect results in an H_2/O_2 ratio lower than 2; (c) at the shock front, where the H_2/O_2 ratio reaches its peak; and (d) upstream of the shock. The distributions have been slightly smoothed using a Gaussian filter ($\sigma = 1$) to enhance clarity.

1.25 μm, slightly larger than the reactive case. Specieswise shock thickness can be computed based on the velocity profiles in Figs. 4(c) and 4(d). In the reactive case, the shock thickness is 1.38 μm for H_2, whereas it is 0.95 μm for O_2. In the inert case, these values are, respectively, 1.48 and 1.04 μm. The reduction of the shock thickness with reaction and the smaller shock thickness of O_2 than H_2 are consistent with the classical theories that the shock thickness is inversely correlated with both the shock strength and diffusivity [73].

2. Velocity distributions across the shock front

To further characterize the nonequilibrium behavior induced by the shock wave, we analyze the distribution of translational velocities of H_2 and O_2 molecules in both reactive and inert cases at several locations relative to the shock front. Figure 5 presents the velocity distributions in the z direction of the center of mass for H_2 and O_2 at various locations relative to the shock front. Upstream (d) and downstream (a) of the shock, the velocity of both species exhibit a Maxwell-Boltzmann distribution, with mean velocities centered around zero (for the stationary

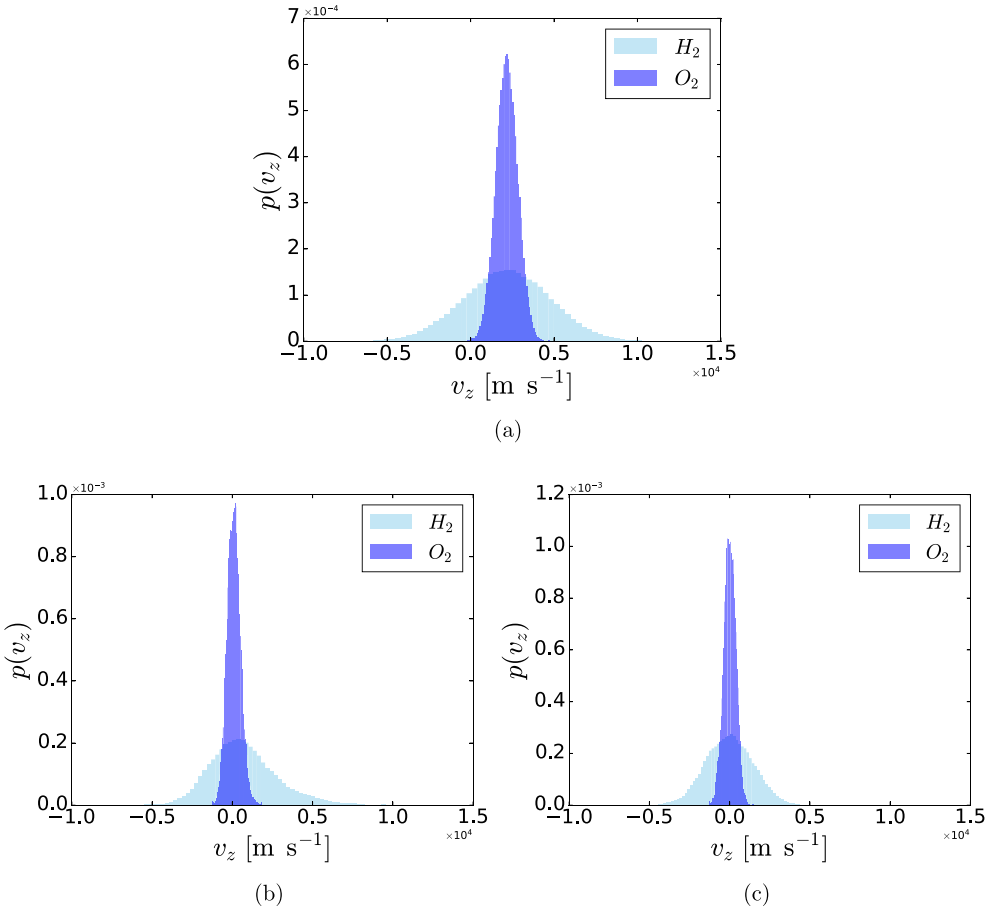

FIG. 6. Velocity distribution in the z direction of the center of mass for H_2 and O_2 in the inert case (a) downstream of the shock front, (b) at the shock front, where the H_2/O_2 ratio reaches its peak, and (c) upstream of the shock. The distributions have been slightly smoothed using a Gaussian filter ($\sigma = 1$) to enhance clarity.

preshock gas) and the piston velocity (for the postshock gas), respectively. The variance of these distributions corresponds to the expected thermal equilibrium temperature, indicating that the flow in these regions is in a near-equilibrium state. In the region immediately after the shock (b), the velocity also follows a Maxwell-Boltzmann distribution, suggesting that the demixing observed in the species concentration does not significantly affect the velocity distribution. In contrast, at the shock front (c), where the H_2/O_2 ratio reaches its peak, the velocity distribution deviates from the Maxwell-Boltzmann form. The distribution appears asymmetric and exhibits a bimodal structure. These results are consistent with previous studies of inert shock waves [54] reporting velocity distributions upstream, downstream, and at the shock front. Their study revealed similar trends, showing Maxwell-Boltzmann distributions before and after the shock, while highlighting deviations and bimodal structures at the shock front.

Figure 6 shows the velocity distributions in the z direction of the center of mass for H_2 and O_2 in the inert case, at different locations relative to the shock front. Similar to the reactive case, the velocity distributions upstream (c) and downstream (a) of the shock exhibit a Maxwell-Boltzmann profile, with mean velocities centered around zero and the piston velocity, respectively. Likewise,

at the shock front (b), the velocity distribution deviates from a pure Maxwell-Boltzmann profile, displaying a bimodal structure similar to that observed in the reactive case.

Therefore, in both the reactive and inert cases, the velocity distributions follow a Maxwell-Boltzmann distribution whether the concentrations are stoichiometric or not, and only at the shock front does a bimodal distribution appear. Chemical reactions, therefore, have only a negligible effect on the relaxation of molecular velocities toward equilibrium.

3. Mean postshock particle velocity

To gain further insights into the nonequilibrium transport that leads to the unique shock substructure, we analyze the streamwise particle velocities of H and O atoms immediately after their interactions with the H_2 shock front. To obtain the postshock particle velocities, all molecular trajectories were first time-aligned so that $t = 0$ corresponds to the instant each particle experiences the shock. This alignment ensures that the extracted velocity traces reflect the statistical ensemble of the shock response in time. The shock thickness measured for H_2 is used to determine the exit time for H_2, while the shock thickness measured for O_2 is used to determine the exit time for O_2. This approach is justified by the substantial mass difference between H_2 and O_2, as the H_2 shock may not impart sufficient momentum to O_2 to trigger shock compression.

The ensemble-averaged streamwise particle velocities of the H and O atoms are, respectively, plotted in Figs. 7(a) and 7(b). In each plot, the results of the reactive and inert cases are compared, along with the piston velocity. The insets present zoom-in views near the shock event ($t_s \approx 0$). The shock residence time τ_r (average time taken to exit the shock region) and the mean free time (average time taken to travel mean free path) τ_m are denoted using $\diamond$ and $\star$, respectively. In the reactive case, $\tau_r = 2.02$ ns for H, whereas $\tau_r = 0.78$ ns for O. In the inert case, the corresponding values are $\tau_r = 2.57$ and 1.21 ns, respectively. In the reactive case, τ_m is estimated at $(T, P) \approx (5.5T_0, 30P_0)$ as $\tau_m \approx 6.0 \times 10^{-3}$ ns for H and 8.1×10^{-3} ns for O. In the inert case, $(T, P) \approx (3.3T_0, 17P_0)$ is used to obtain $\tau_m \approx 8.2 \times 10^{-3}$ ns for H and $\tau_m \approx 1.11 \times 10^{-2}$ ns for O, based on collision estimates for binary gas mixtures [74]. The overall lower values of τ_r in the reactive case than in the inert case are consistent with the faster shock speed and the smaller shock thickness of the reactive shock wave compared to the inert one. For both reactive and inert cases, the initial mean velocities (ballistic velocities) of H and O atoms are greater and smaller than the mixture's shock speed [Figs. 7(a) and 7(b)]. The ballistic velocities can be easily interpreted by molecular collision; H, which is lighter than the average molecular weight of the mixture, gains a larger velocity than the mixture's impact speed (shock speed), and the opposite occurs to O, which is heavier than the mixture. In the reactive case, the velocity of H experiences a rapid decay to reach the postshock velocity in Fig. 4(c) at $t \approx 0.2$ ns and then experiences a milder and monotonous decline. Over a sufficient period, the velocity is expected to match the piston speed. For the inert case, the velocity of H rapidly decreases to a minimum below the piston speed at $t \approx 0.4$ ns, followed by a mild increase to the piston speed. The behavior of the O velocity is straightforward; in both reactive and inert cases, the velocities smoothly increase to reach the equilibrium velocity. The velocity damping of H below the shock speed in the inert case can be considered a process of momentum relaxation with slower molecules (e.g., O_2 molecules slower than the piston speed). Similar decay and reacceleration of the velocity during the relaxation period may occur in the reactive case, but the minimum is not visible likely due to the cancellation by the negative slope of the equilibrium velocity [Fig. 4(c)]. The evolution of the ratio of the H and O velocities is plotted in Fig. 7(c) for both reactive and inert cases. In both cases, a monotonic decrease in the ratio is observed at around 0.5 ns, indicating relaxation among species within this timescale. This species relaxation thus occurs within the shock wave, as indicated by the shock residence times greater than 0.5 ns. The particle velocities are clearly consistent with the observed shock structure. The faster ballistic velocities of H than those of O lead to the formation of the H_2 shock front ahead of O_2. The species velocities are relaxed behind the O_2 shock front but within the shock region of the mixture, and reactions may occur there. We emphasize that these nonequilibrium effects, including the shock front separation, can be

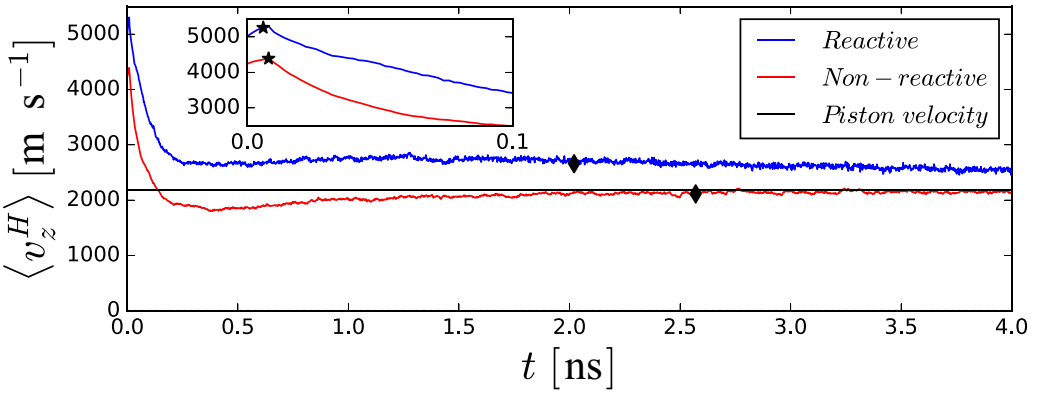

(a)

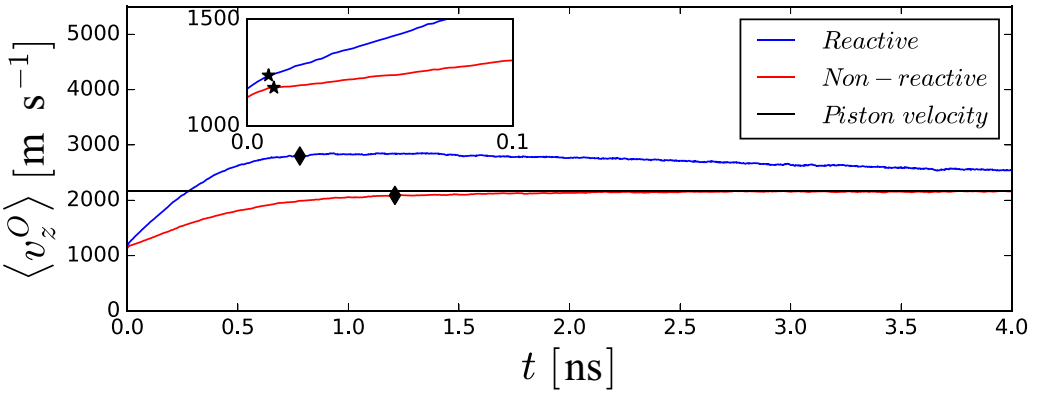

(b)

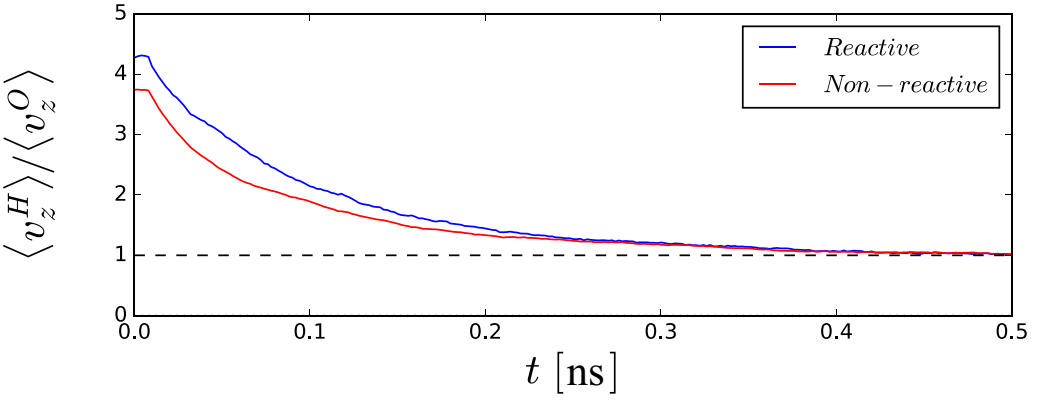

(c)

FIG. 7. Evolution of the ensemble-averaged, streamwise particle velocities, $\langle v_z \rangle$, for hydrogen atoms H (a) and oxygen atoms O (b), after the shock impact, in reactive (blue) and inert (red) cases. Ratio of the mean velocities (c) with and without reactions.

unique to H_2/O_2 mixture that poses a large mass ratio, and they can be enhanced with the shock strength.

IV. CONCLUSIONS

In this study, nonequilibrium MD simulation of a reactive shock wave was performed in a gaseous stoichiometric H_2/O_2 mixture using the ReaxFF potential. The results show substructures in the shock wave in that H_2 is compressed ahead of O_2 to form distinct shock fronts. Notably, the dissociation of H_2 begins right behind the H_2 shock front before the O_2 shock front, whereas dissociation of O_2 occurs only behind the O_2 shock front. Therefore, the main exothermic chemical reactions are triggered only behind the O_2 shock front. Comparisons with the synthetic, inert shock wave indicate that the small H_2 to O_2 mass ratio causes the separation of shock fronts regardless of chemistry, like those observed in shocks of rarefied binary gases, and the velocities of the species relax before leaving the shock region. Although the MD shock speed has not yet been fully equilibrated, the postshock flow field already exhibits a ZND-like structure. The shock structures and their formation mechanisms identified in the present simulation may thus hold for reactive shock waves in general stoichiometric H_2/O_2 mixtures. These results characterize the nonequilibrium H_2/O_2 shock dynamics, showing that reactions are present but not as active as they were without the nonequilibrium separation of shock fronts. The insights gained in this study may motivate generalization of this MD analysis for SICR in different species mass ratios of energetic gaseous mixtures at various ambient conditions.

ACKNOWLEDGMENTS

T.M.-O. acknowledges the Apollo 11 Postdoctoral Fellowship through the Purdue School of Aeronautics and Astronautics. This work is supported by SRB Co. Inc. This work used Delta GPU at the National Center for Supercomputing Applications (NCSA) through allocation PHY250084 from the Advanced Cyberinfrastructure Coordination Ecosystem: Services & Support (ACCESS [75]) program, which is supported by U.S. National Science Foundation Grants No. 2138259, No. 2138286, No. 2138307, No. 2137603, and No. 2138296.

DATA AVAILABILITY

The data that support the findings of this article are not publicly available upon publication because it is not technically feasible and/or the cost of preparing, depositing, and hosting the data would be prohibitive within the terms of this research project. The data are available from the authors upon reasonable request.

APPENDIX A: COMPARISONS WITH THE ZND MODEL

In this Appendix, we provide supplemental details on the comparison of our MD results and the ZND solutions obtained using the mechanism of Hong *et al.* [69] within the SDToolbox framework [70]. Two cases of ZND calculation were set up for a stoichiometric H_2/O_2 mixture at 1 atm and an initial temperature of 500 K. In the first case (fixed u_p), the shock speed is set such that the downstream gas velocity equals the piston speed. In the second case (fixed u_s), the shock speed is set to match the MD shock speed. For the first ZND case, the predicted piston velocity is $2602\,\mathrm{m\,s^{-1}}$, which is higher than the MD piston velocity ($2175.18\,\mathrm{m\,s^{-1}}$). For the second ZND case, the predicted shock velocity is approximately $3185\,\mathrm{m\,s^{-1}}$, which is smaller than the MD shock speed ($3504.55\,\mathrm{m\,s^{-1}}$ at $t = 20\,\mathrm{ns}$). Figure 8 shows the normalized profiles of (a) density, (b) pressure, (c) z velocity, and (d) temperature of the two ZND solutions (fixed u_p and fixed u_s) along with MD results. The origin corresponds to the density peak point in the postshock region. Overall, the plots of the MD solution show similar tendencies of growth/decay to those of the ZND solutions. The MD solution is highly compressed compared to the ZND solutions, as explained by the proximity

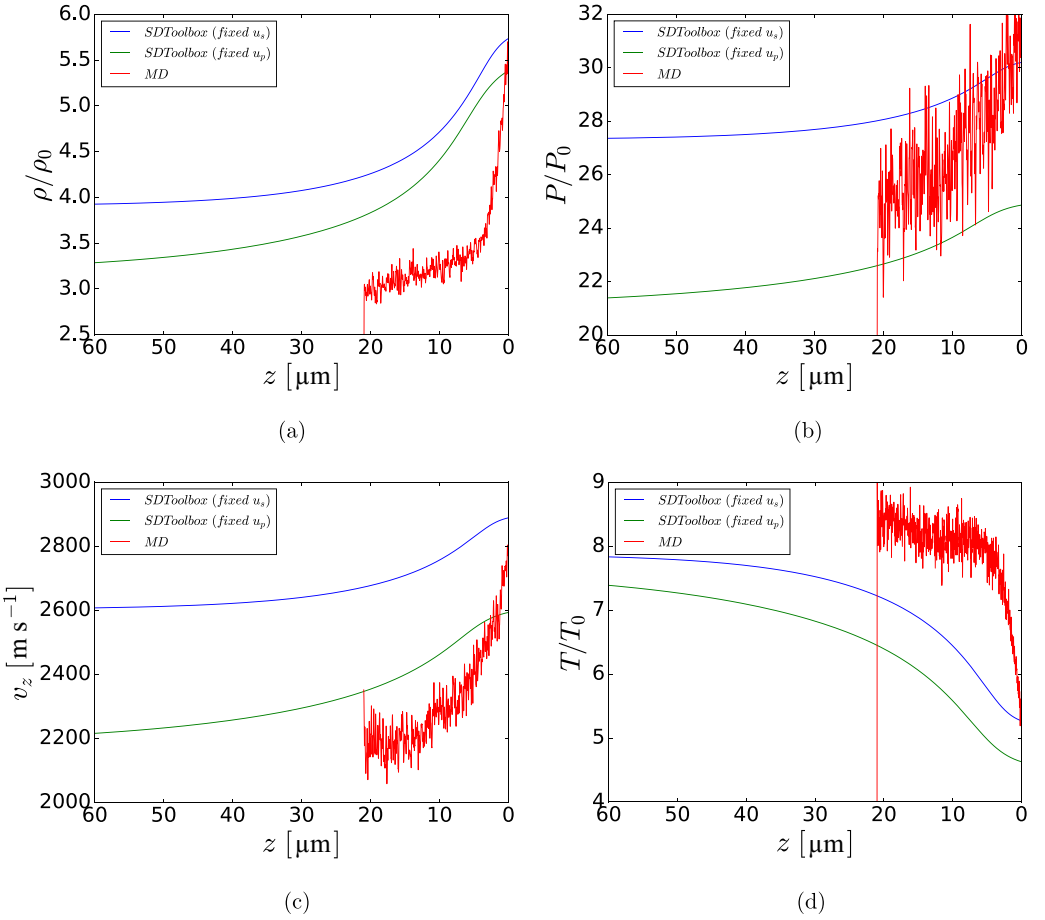

FIG. 8. Normalized profiles of (a) density, (b) pressure, (c) z velocity, and (d) temperature for a stoichiometric H_2/O_2 mixture, comparing ZND solutions under fixed downstream gas velocity (fixed u_p) and fixed shock propagation speed (fixed u_s) with MD results. ZND profiles are shown from the end of the initial induction plateau, and MD results are shown from the location of the density peak.

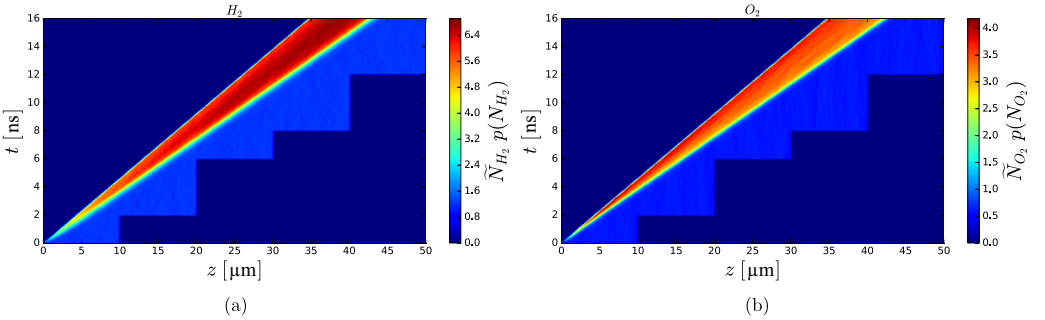

FIG. 9. Contour of the space-time distribution for each species in an inert H_2/O_2 mixture during 16 ns for (a) H_2 and (b) O_2.

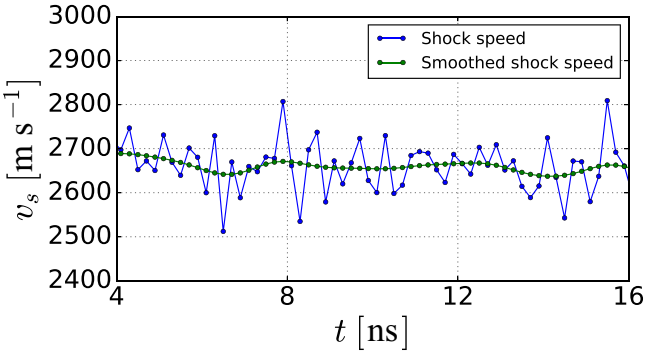

FIG. 10. Time evolution of the shock propagation speed in the inert case, showing both the raw computed shock speed (blue) and the smoothed shock speed (green).

between the piston and the shock in the MD state. As expected, the MD solutions at the immediate postshock point (origin) are closer to those of the first ZND solution than the second one, while the MD quantities at the piston are closer to the second ZND solution except for the temperature. It is implied that the MD solution approaches the second ZND solution if the MD simulation is continued sufficiently long to extend the postshock region and the pressure is lowered there.

APPENDIX B: SHOCK EVOLUTION IN THE INERT CASE

Figure 9 presents two-dimensional histograms displaying the spatial and temporal distribution of each species within an inert H_2/O_2 mixture over 16 ns for (a) H_2 and (b) O_2. We can observe that the shock formation stabilizes shortly after initiation, occurring within just a few nanoseconds. Figure 10 shows that the shock speed remains nearly constant, fluctuating around a mean value of 2656.22 m s^{-1}, smaller than that of the reactive case, as expected by the Ranking-Hugoniot condition in the absence of exothermic heat release.

[1] J. Meyer and A. Oppenheim, On the shock-induced ignition of explosive gases, in *Symposium (International) on Combustion* (Elsevier, Amsterdam, 1971), Vol. 13, pp. 1153–1164.
[2] J. Ahuja, S. Tiwari, and D. Singh, Hypersonic shock-induced combustion in a hydrogen-air system, AIAA J. **33**, 173 (1995).
[3] S. Yungster and M. J. Rabinowitz, Computation of shock-induced combustion using a detailed methane-air mechanism, J. Propul. Power **10**, 609 (1994).
[4] E. S. Oran and V. N. Gamezo, Origins of the deflagration-to-detonation transition in gas-phase combustion, Combust. Flame **148**, 4 (2007).
[5] A. Y. Poludnenko, T. A. Gardiner, and E. S. Oran, Spontaneous transition of turbulent flames to detonations in unconfined media, Phys. Rev. Lett. **107**, 054501 (2011).
[6] M.-H. Wu, M. Burke, and R. Yetter, Flame acceleration and the transition to detonation of stoichiometric ethylene/oxygen in microscale tubes, Proc. Combust. Inst. **31**, 2429 (2007).
[7] L. Meng, Q.-G. Song, C. Yao, L. Zhang, and S.-p. Pang, Chemical reaction mechanisms and models of energetic materials: A perspective, Energetic Mater. Front. **6**, 129 (2025).
[8] T. Yamada, A. K. Hayashi, E. Yamada, N. Tsuboi, V. E. Tangirala, and T. Fujiwara, Detonation limit thresholds in H_2/O_2 rotating detonation engine, Combust. Sci. Technol. **182**, 1901 (2010).
[9] C. Huete, A. L. Sánchez, and F. A. Williams, Diffusion-flame ignition by shock-wave impingement on a hydrogen–air supersonic mixing layer, J. Propul. Power **33**, 256 (2017).

[10] A. K. Hayashi, N. Tsuboi, and E. Dzieminska, Numerical study on JP-10/air detonation and rotating detonation engine, AIAA J. **58**, 5078 (2020).
[11] A. Robert, S. Richard, O. Colin, and T. Poinsot, LES study of deflagration to detonation mechanisms in a downsized spark ignition engine, Combust. Flame **162**, 2788 (2015).
[12] J. Crane, X. Shi, A. V. Singh, Y. Tao, and H. Wang, Isolating the effect of induction length on detonation structure: Hydrogen–oxygen detonation promoted by ozone, Combust. Flame **200**, 44 (2019).
[13] D. A. Rosato, M. Thornton, J. Sosa, C. Bachman, G. B. Goodwin, and K. A. Ahmed, Stabilized detonation for hypersonic propulsion, Proc. Natl. Acad. Sci. USA **118**, e2102244118 (2021).
[14] K. Iwata, S. Suzuki, R. Kai, and R. Kurose, Direct numerical simulation of detonation–turbulence interaction in hydrogen/oxygen/argon mixtures with a detailed chemistry, Phys. Fluids **35**, 046107 (2023).
[15] M. D. Frederick, R. M. Gejji, J. E. Shepherd, and C. D. Slabaugh, Statistical analysis of detonation wave structure, Proc. Combust. Inst. **39**, 2847 (2023).
[16] M. Oevermann, Numerical investigation of turbulent hydrogen combustion in a SCRAMJET using flamelet modeling, Aerospace Sci. Technol. **4**, 463 (2000).
[17] D. Cecere, A. Ingenito, E. Giacomazzi, L. Romagnosi, and C. Bruno, Hydrogen/air supersonic combustion for future hypersonic vehicles, Int. J. Hydrogen Energy **36**, 11969 (2011).
[18] P. Clavin and G. Searby, *Combustion Waves and Fronts in Flows: Flames, Shocks, Detonations, Ablation Fronts and Explosion of Stars* (Cambridge University Press, Cambridge, UK, 2016).
[19] S. Frolov, V. Aksenov, V. Ivanov, and I. Shamshin, Large-scale hydrogen–air continuous detonation combustor, Int. J. Hydrogen Energy **40**, 1616 (2015).
[20] A. Mura, A. Techer, and G. Lehnasch, Analysis of high-speed combustion regimes of hydrogen jet in supersonic vitiated airstream, Combust. Flame **239**, 111552 (2022).
[21] R. Becker, Stosswelle und detonation, Z. Phys. **8**, 321 (1922).
[22] L. Thomas, Note on Becker's theory of the shock front, J. Chem. Phys. **12**, 449 (1944).
[23] F. S. Sherman, Shock-wave structure in binary mixtures of chemically inert perfect gases, J. Fluid Mech. **8**, 465 (1960).
[24] C. J. Greenshields and J. M. Reese, The structure of shock waves as a test of Brenner's modifications to the Navier–Stokes equations, J. Fluid Mech. **580**, 407 (2007).
[25] H. M. Mott-Smith, The solution of the Boltzmann equation for a shock wave, Phys. Rev. **82**, 885 (1951).
[26] T. Tokumasu and Y. Matsumoto, Dynamic molecular collision (DMC) model for rarefied gas flow simulations by the DSMC method, Phys. Fluids **11**, 1907 (1999).
[27] S. Kosuge, K. Aoki, and S. Takata, Shock-wave structure for a binary gas mixture: finite-difference analysis of the Boltzmann equation for hard-sphere molecules, Eur. J. Mech. B Fluids **20**, 87 (2001).
[28] A. Raines, Study of a shock wave structure in gas mixtures on the basis of the Boltzmann equation, Eur. J. Mech. B Fluids **21**, 599 (2002).
[29] G. Bird, The structure of normal shock waves in a binary gas mixture, J. Fluid Mech. **31**, 657 (1968).
[30] M. Y. Timokhin, Y. A. Bondar, A. Kokhanchik, M. Ivanov, I. Ivanov, and I. Kryukov, Study of the shock wave structure by regularized Grad's set of equations, Phys. Fluids **27**, 037101 (2015).
[31] I. D. Boyd, Computation of hypersonic flows using the direct simulation Monte Carlo method, J. Spacecr. Rockets **52**, 38 (2015).
[32] P. Valentini, T. E. Schwartzentruber, J. D. Bender, and G. V. Candler, Dynamics of nitrogen dissociation from direct molecular simulation, Phys. Rev. Fluids **1**, 043402 (2016).
[33] I. Borges Sebastião, M. Kulakhmetov, and A. Alexeenko, DSMC study of oxygen shockwaves based on high-fidelity vibrational relaxation and dissociation models, Phys. Fluids **29**, 017102 (2017).
[34] T. E. Schwartzentruber, M. S. Grover, and P. Valentini, Direct molecular simulation of nonequilibrium dilute gases, J. Thermophys. Heat Transfer **32**, 892 (2018).
[35] M. S. Grover, E. Torres, and T. E. Schwartzentruber, Direct molecular simulation of internal energy relaxation and dissociation in oxygen, Phys. Fluids **31**, 076107 (2019).
[36] S. S. Sawant, D. A. Levin, and V. Theofilis, A kinetic approach to studying low-frequency molecular fluctuations in a one-dimensional shock, Phys. Fluids **33**, 104106 (2021).

[37] H. Carlson, R. Roveda, I. Boyd, and G. Candler, A hybrid CFD-DSMC method of modeling continuum-rarefied flows, in *42nd AIAA Aerospace Sciences Meeting and Exhibit* (AIAA, Reston, VA, 2004), p. 1180.

[38] Y. A. Bondar, K. Maruta, and M. S. Ivanov, Hydrogen-oxygen detonation study by the DSMC method, in *27th International Symposium on Rarefied Gas Dynamics* (American Institute of Physics, Melville, NY, 2011), pp. 1209–1214.

[39] I. B. Sebastião, L. Qiao, and A. Alexeenko, Direct simulation Monte Carlo modeling of $H_2 - O_2$ deflagration waves, Combust. Flame **198**, 40 (2018).

[40] S. Trivedi, J. S. Salinas, J. K. Harvey, A. Y. Poludnenko, and J. H. Chen, Simulations of hydrogen-air detonations using direct simulation Monte Carlo, Combust. Flame **279**, 114333 (2025).

[41] N. G. Hadjiconstantinou, A. L. Garcia, M. Z. Bazant, and G. He, Statistical error in particle simulations of hydrodynamic phenomena, J. Comput. Phys. **187**, 274 (2003).

[42] D. H. Robertson, D. W. Brenner, and C. T. White, Split shock waves from molecular dynamics, Phys. Rev. Lett. **67**, 3132 (1991).

[43] T. C. Germann, B. L. Holian, P. S. Lomdahl, and R. Ravelo, Orientation dependence in molecular dynamics simulations of shocked single crystals, Phys. Rev. Lett. **84**, 5351 (2000).

[44] E. Jaramillo, T. D. Sewell, and A. Strachan, Atomic-level view of inelastic deformation in a shock loaded molecular crystal, Phys. Rev. B **76**, 064112 (2007).

[45] K. V. Reddy, C. Deng, and S. Pal, Dynamic characterization of shock response in crystalline-metallic glass nanolaminates, Acta Mater. **164**, 347 (2019).

[46] P. Wen, G. Tao, D. E. Spearot, and S. R. Phillpot, Molecular dynamics simulation of the shock response of materials: A tutorial, J. Appl. Phys. **131**, 051101 (2022).

[47] M. Elert, D. Robertson, J. Barrett, and C. White, Molecular dynamics study of reaction zone properties in chemically sustained shock waves, in *Proceedings of the Conference of the American Physical Society Topical Group on Shock Compression of Condensed Matter* (American Institute of Physics, MD, USA, 1996), Vol. 370, pp. 183–186.

[48] A. J. Heim, N. Grønbech-Jensen, T. C. Germann, E. M. Kober, B. L. Holian, and P. S. Lomdahl, Influence of interatomic bonding potentials on detonation properties, Phys. Rev. E **76**, 026318 (2007).

[49] M. Am-Shallem, Y. Zeiri, S. V. Zybin, and R. Kosloff, Molecular dynamics simulations of weak detonations, Phys. Rev. E **84**, 061122 (2011).

[50] M. M. Islam and A. Strachan, Decomposition and reaction of polyvinyl nitrate under shock and thermal loading: A ReaxFF reactive molecular dynamics study, J. Phys. Chem. C **121**, 22452 (2017).

[51] Y. Xiong, S. Xiao, H. Deng, W. Zhu, and W. Hu, Investigation of the shock-induced chemical reaction (SICR) in Ni+Al nanoparticle mixtures, Phys. Chem. Chem. Phys. **19**, 17607 (2017).

[52] H. Liu, Y. He, J. Li, Z. Zhou, Z. Ma, S. Liu, and X. Dong, ReaxFF molecular dynamics simulations of shock induced reaction initiation in TNT, AIP Adv. **9**, 015202 (2019).

[53] R. Murugesan and M. Radulescu, The influence of non-equilibrium translational effects on reactive dynamics during shock to detonation transition using molecular dynamics, in *29th ICDERS* (SNU Siheung, Korea, 2023).

[54] A. S. Jayaraman, E. S. Genter, W. Dong, and H. Wang, Collision enhancement in shocks and its implication on gas-phase detonations: A molecular dynamics and gas-kinetic theory study, Proc. Combust. Inst. **40**, 105741 (2024).

[55] S. Pal and N. Mitra, Shock wave propagation through air: a reactive molecular dynamics study, Proc. R. Soc. A **477**, 20200676 (2021).

[56] A. C. Van Duin, S. Dasgupta, F. Lorant, and W. A. Goddard, ReaxFF: a reactive force field for hydrocarbons, J. Phys. Chem. A **105**, 9396 (2001).

[57] Y. B. Zel'dovich, On the theory of the propagation of detonation in gaseous systems, Zh. Eksp. Teor. Fiz. **10**, 542 (1940).

[58] J. von Neumann, Theory of detonation waves, *Progress Report to the National Defense Research Committee, OSRD-549* (Office of Scientific Research and Development, Washington, DC, 1942).

[59] W. Döring, Über den detonationsvorgang in gasen, Ann. Phys. **435**, 421 (1943).

[60] A. P. Thompson, H. M. Aktulga, R. Berger, D. S. Bolintineanu, W. M. Brown, P. S. Crozier, P. J. In't Veld, A. Kohlmeyer, S. G. Moore, T. D. Nguyen *et al.*, LAMMPS-a flexible simulation tool for particle-based materials modeling at the atomic, meso, and continuum scales, Comput. Phys. Commun. **271**, 108171 (2022).

[61] K. Chenoweth, A. C. van Duin, and W. A. Goddard, ReaxFF reactive force field for molecular dynamics simulations of hydrocarbon oxidation, J. Phys. Chem. A **112**, 1040 (2008).

[62] S. Nosé, A unified formulation of the constant temperature molecular dynamics methods, J. Chem. Phys. **81**, 511 (1984).

[63] L. Verlet, Computer "experiments" on classical fluids. I. thermodynamical properties of Lennard-Jones molecules, Phys. Rev. **159**, 98 (1967).

[64] Y. N. Denisov and Y. K. Troshin, Structure of gaseous detonation in tubes, Zh. Tekh. Fiz. **450** (1960) [Sov. Phys. Tech. Phys. **5**, 419 (1960)].

[65] D. Desbordes, Aspects stationnaires et transitoires de la détonation dans les gaz: relation avec la structure cellulaire du front, Ph.D. thesis, Poitiers, 1990.

[66] R. Zitoun, D. Desbordes, C. Guerraud, and B. Deshaies, Direct initiation of detonation in cryogenic gaseous $H_2 - O_2$ mixtures, Shock Waves **4**, 331 (1995).

[67] V. I. Manzhalei, V. V. Mitrofanov, and V. A. Subbotin, Measurement of inhomogeneities of a detonation front in gas mixtures at elevated pressures, Combust. Explos. Shock Waves **10**, 89 (1974).

[68] V. Monnier, Aspects tridimensionnels de la détonation cellulaire: des observations expérimentales et un modèle, Ph.D. thesis, ISAE-ENSMA Ecole Nationale Supérieure de Mécanique et d'Aérotechique-Poitiers, 2023.

[69] Z. Hong, D. F. Davidson, and R. K. Hanson, An improved H_2/O_2 mechanism based on recent shock tube/laser absorption measurements, Combust. Flame **158**, 633 (2011).

[70] S. T. Kao, J. L. Ziegler, N. P. Bitter, B. E. Schmidt, J. M. Lawson, and J. E. Shepherd, Numerical tools for shock and detonation wave modeling, GALCIT Report FM2018.001, California Institute of Technology, Pasadena, CA, 2023, http://shepherd.caltech.edu/EDL/PublicResources/sdt/.

[71] L. Prandtl, Zur theorie des verdichtungsstosses, Z. Gesamte Turbinen. **3**, 241 (1906).

[72] Q. Li, J. Zeng, and L. Wu, Kinetic modelling of rarefied gas mixtures with disparate mass in strong non-equilibrium flows, J. Fluid Mech. **1001**, A5 (2024).

[73] W. G. Vincenti and C. H. Kruger, Jr., *Introduction to Physical Gas Dynamics* (Wiley, New York, 1965), p. 538.

[74] K. J. Laidler and J. M. Meiser, *Physical Chemistry* (Benjamin/Cummings, San Francisco, CA, 1982), pp. 18–19.

[75] T. J. Boerner, S. Deems, T. R. Furlani, S. L. Knuth, and J. Towns, ACCESS: Advancing innovation: NSF's advanced cyberinfrastructure coordination ecosystem: Services & support, in *Practice and Experience in Advanced Research Computing 2023: Computing for the Common Good* (Association for Computing Machinery, Portland, OR, 2023), pp. 173–176.